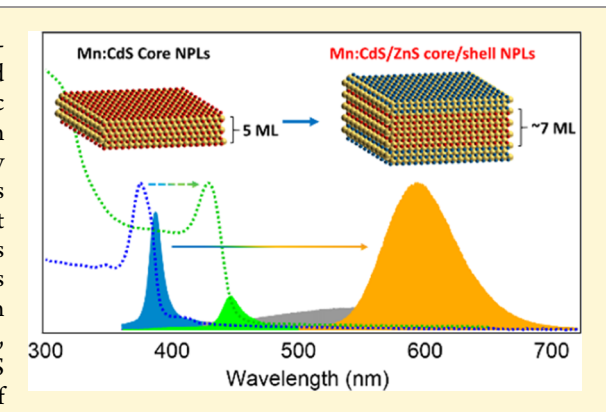
Downloaded via UNIV OF MAINE on April 19, 2019 at 14:42:27 (UTC). See https://pubs.acs.org/sharingguidelines for options on how to legitimately share published articles.

Exciton Energy Shifts and Tunable Dopant Emission in Manganese-Doped Two-Dimensional CdS/ZnS Core/Shell Nanoplatelets

Andrew H. Davis,[†] Elan Hofman,[†] Kevin Chen,[†] Zhi-Jun Li,[†] Alex Khammang,[‡] Hediyeh Zamani,[†] John M. Franck,[†] Mathew M. Maye,[†] Robert W. Meulenberg,[‡] and Weiwei Zheng*,[†]

Supporting Information

ABSTRACT: The ability to dope transition-metal ions into semiconductor nanocrystals (NCs) allows for the introduction and exploitation of new extrinsic properties in the original intrinsic material. Although the synthesis of doped zero-dimensional quantum dots and one-dimensional nanorods/nanowires has been widely reported, transition-metal ion-doped two-dimensional (2D) NCs have been less explored. In this study, we developed a one-pot synthesis of Mn²⁺-doped 2D CdS (i.e., Mn:CdS) nanoplatelets (NPLs). Successful Mn doping inside the CdS NPL lattice was confirmed by electron paramagnetic resonance and X-ray diffraction measurements. Surprisingly, only CdS photoluminescence (PL), without contribution from Mn PL, was observed in the Mn:CdS NPLs, regardless of Mn doping concentration. To address the issue of poor thermal stability and improve the optical properties of the 2D



Mn:CdS NPLs, we synthesized ZnS shell-passivated Mn:CdS/ZnS core/shell NPLs using a single-source shelling precursor method, which allows for ZnS surface passivation of NPLs at relatively low temperatures, while being thermally adaptable to ensure minimal NPL degradation. An extremely large exciton red shift (~420 meV), upon ZnS shell passivation, was observed because of the increased effective thickness of the CdS core NPLs. Steady-state and time-resolved emission measurements indicate that the host-dopant energy-transfer efficiency and Mn-Mn interactions within the 2D Mn:CdS/ZnS core/shell NPLs can be fine-tuned via the dopant concentration, resulting in an intense Mn PL as well as tunable dual-band emission from the host NPLs and Mn dopants. Magnetic measurements indicate intrinsic spin states in the 2D NPLs and complex magnetic interactions at high doping concentrations, including antiferromagnetic exchange between dopants and possible dopant-surface state interaction.

■ INTRODUCTION

Semiconductor nanocrystals (NCs) have been extensively studied for applications in green energy harvesting and biological research, leading to the development of a wide array of high-quality NCs with varying size, shape, and composition. With the incorporation of transition-metal ions as dopants inside NCs, new optical, electrical, and magnetic properties can be achieved and controlled based on dopant concentration. 10-17 For example, a distinct dopant emission can be observed in many Mn2+-doped II-VI group semiconductor NCs (including CdS, ZnSe, ZnS, etc.)^{18–21} and perovskite NCs²²⁻²⁴ from the efficient NC-to-dopant energy transfer. Doped NCs, therefore, are promising materials for applications in spintronics, photovoltaics, and quantum computing. ²⁵⁻³⁰ Compared with doped zero-dimensional (0D) and one-dimensional (1D) NCs, doped two-dimensional (2D) nanoplatelets (NPLs) can offer the possibility of enhanced optical lasing, anisometric magnetics, and polarized light emission utilizing the narrow emission band and ultrafast

charge carrier recombination. 17,31-35 Currently, there are many reports on transition-metal-doped 0D spherical NCs by nucleation doping,³⁶ growth doping,³⁷ predoped single-source precursor,^{38,39} and ion exchange and diffusion.⁴⁰ Despite doped 0D NCs being widely studied,²⁶ doped anisotropic NCs, especially 2D NCs, have been far less explored.

To date, only a few Mn2+-doped 2D II-VI metal chalcogenide NCs have been reported, 17,41-43 with these few displaying limited optical properties. Furthermore, direct doping into 2D CdS NPLs has not yet been reported, with multiple opting to dope into a CdS shell surrounding 2D CdSe core NPLs. 41,42 In general, the limited reports on doped 2D metal chalcogenides reflect the challenge in synthesizing doped 2D NCs, which might be due to the anisotropic growth of the NCs leading to limited growing facet with sufficient binding

Received: January 1, 2019 Revised: March 15, 2019 Published: March 18, 2019

Department of Chemistry, Syracuse University, Syracuse, New York 13244, United States

^{*}Laboratory for Surface Science and Technology and Department of Physics and Astronomy, University of Maine, Orono, Maine 04469, United States

energy for dopant ion addition⁴⁴ as well as the prevalence of dopant ejection by the self-annealing effect.^{45,46} In addition, the large surface-to-volume ratio of 2D NCs makes maintaining thermodynamic and environmental stability problematic. The relatively poor thermal stability of 2D NCs could make the solution-phase doping at high temperature very challenging.⁴⁷ For example, cadmium chalcogenides are known for their poor thermal and environmental stability in which loss of structural integrity ensues, leading to quenched photoluminescence (PL) at elevated temperatures.⁴⁷

In this study, we developed a one-pot synthesis for Mn²⁺-doped 2D CdS (i.e., Mn:CdS) NPLs followed by ZnS shell passivation for Mn:CdS/ZnS core/shell NPLs with enhanced thermal stability. Interestingly, the Mn PL is only observed in the 2D Mn:CdS/ZnS core/shell NPLs, while it is absent in the 2D Mn:CdS NPLs. The host—dopant energy transfer and Mn—Mn interactions of these doped core/shell NPLs are dopant concentration-dependent, allowing for a tunable dualband emission from the host NPLs and Mn dopants. Through dopant introduction and surface modification, we have synthesized not only the first 2D Mn:CdS NPLs but also the first 2D Mn:CdS/ZnS core/shell NPLs with enhanced optical properties.

■ RESULTS AND DISCUSSION

In this study, we successfully synthesized Mn²⁺-doped 2D CdS NPLs by reacting manganese nitrate and cadmium myristate with sulfur precursor in ODE at 200 °C (see details in the Experimental Section). We further grew a ZnS shell on the Mn:CdS NPLs to synthesize 2D Mn:CdS/ZnS core/shell NPLs, using a single-source shelling precursor (SSSP) method by thermal decomposition of a single precursor, zinc diethyldithiocarbamate (Zn(DDTC)₂),⁴⁸ in a solution of ODE, and oleylamine (OAm) (Experimental Section). The single-source precursor supplies both the Zn and S necessary for shelling, which slowly breaks down at around 100 °C allowing for the passivation of the NPL surface with ZnS at relatively low temperatures. 49 We found that the SSSP method is efficient for NPL shell passivation, as relatively low reaction temperatures can be employed (120-220 °C), while being thermally adaptable for minimal NPL degradation. 48,49 Other shelling temperatures, such as altering the maximum temperature to 200, 240, or 280 °C, were attempted using the SSSP method. However, these conditions were inadequate for proper shell formation. For example, low temperatures such as 200 °C resulted in low PL quantum yield (QY) (Figure S1) of the core/shell NPLs. Higher maximum shelling temperatures such as 240 and 280 $^{\circ}\tilde{C}$ caused thermal degradation and melting of the NPLs, often leading to samples consisting of irregular-shaped 2D NCs, 1D nanorods, and even spherical NCs (Figure S2). Therefore, it is imperative to keep the reaction temperature no higher than 220 °C to avoid NPL degradation as well as no lower than 200 °C to improve optical properties.

Transmission electron microscopy (TEM) images of Mn:CdS core NPLs (Figure 1a ([Mn]: 0%), Figure 1b ([Mn]: 2.5%), and Figure S3a—e ([Mn]: 0–4.7%)) indicate 2D NPLs of a curved structure with ~20 × 50 nm lateral dimensions. The curved appearance of the NPLs is most likely due to the ultrathin CdS NPLs at only 5-monolayer (ML) (~1.45 nm) thickness based on optical data (discussed below), 50 with large surface energy also causing NPL stacking. ZnS shell-passivated NPLs (Figures 1c and S3f—j) are far more

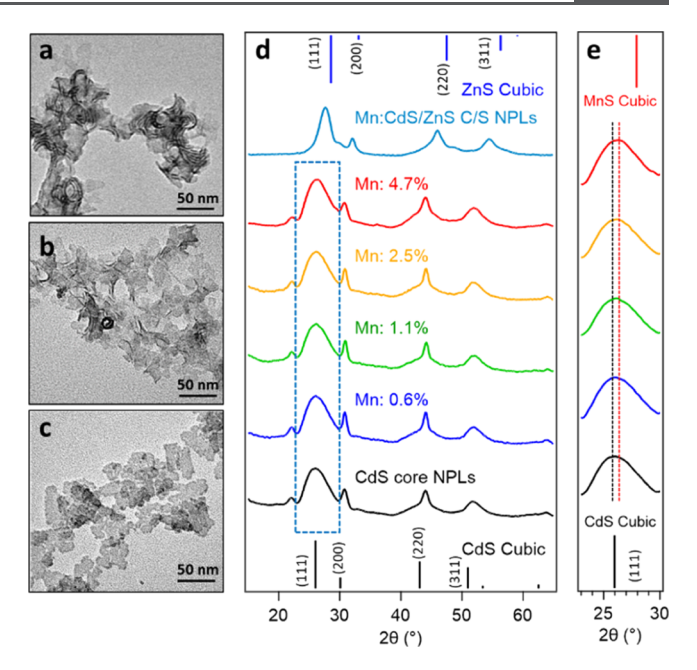


Figure 1. TEM images of (a) 2D CdS NPLs, (b) 2D Mn:CdS NPLs, and (c) 2D Mn:CdS/ZnS core/shell (C/S) NPLs; (d) powder XRD patterns of Mn:CdS core NPLs and Mn:CdS/ZnS core/shell NPLs. (e) Zoomed-in XRD patterns showing peak shifting of the (111) diffraction peak by increasing the Mn-doping concentration.

rigid because of their increased thickness resulting in less NPL stacking and bowing than core NPLs, which might be from the decrease in surface-to-volume ratio and therefore surface energy in the core/shell NPLs. Core/shell NPL lateral dimensions resemble that of the core NPLs; however, thickness comparisons are difficult to discern using TEM imaging. Therefore, atomic force microscopy (AFM) was utilized to determine the thickness of Mn:CdS/ZnS core/shell NPLs and the ZnS shell thickness. Figure S4a displays an AFM image, which exhibits ~3.4 nm thickness of the core/shell NPLs discerned by cross-sectional analysis of individual particles (Figure S4b). According to these results, the thickness of ZnS achieved using the SSSP method is ~2.0 nm. The data in Figure S4b exhibits long flat regions around 3.4 nm in height that stretch for 40-60 nm in position along the Mn:CdS/ZnS core/shell NPLs. The inductively coupled plasma optical emission spectrometry (ICP-OES) data indicates that the doping concentration decreased from 0.6, 1.1, 2.5, and 4.7% in Mn:CdS NPLs to 0.2, 0.4, 0.9, and 1.5% in Mn:CdS/ZnS core/shell NPLs. The partial removal of Mn dopants during ZnS shell passivation of Mn-doped NCs is consistent with previous observations in shell-passivated doped 0D and 1D NCs. 19,37

The powder X-ray diffraction (XRD) of Mn:CdS core NPLs indicates cubic phase CdS. The core NPLs showed a sharp (200) reflection at $2\theta = 30.8^{\circ}$, corresponding to the lateral plane (100) of the 2D NPLs, as previously reported. ^{50,51} The broad (111) diffraction peak of the 2D NPLs can be understood as having a high plane angle offset of 54.7° with respect to the (100) lateral plane, which is nearly parallel with the thickness of the NPLs, causing a broadening effect because of the small size effect. Careful examination of the XRD patterns indicates diffraction peak shifting to higher angles with increasing dopant concentrations (Figure 1d,e). For example, a shift in 2θ of 0.271° along the (111) plane from 0 to 4.7%

doping concentration can be observed, which can be explained by considering compression by 0.017 Å along the (111) lattice plane (Figure S5). The lattice compression can be understood by replacing the larger Cd^{2+} ions (92 pm) with small dopant Mn^{2+} ions (80 pm), suggesting successful incorporation of Mn^{2+} ions inside the host CdS lattice. The small diffraction peak located at 22.1° is attributed to the scattering or diffraction of organic ligands that are present in the reaction. ¹⁸

The XRD pattern of Mn:CdS/ZnS core/shell NPLs (Figures 1d and S6) shift from the original cubic CdS lattice toward a cubic ZnS lattice indicative of successful ZnS shell passivation. The growth of the ZnS shell resulted in the significant narrowing of the (111) diffraction, which could be explained by the significant increase in the thickness of the 2D NPLs from 1.45 to 3.4 nm. No significant peak shift can be observed between core/shell NPLs (Figure S6), showing near-uniform shell passivation of the core Mn:CdS NPLs with no variance based on dopant concentration.

The thermal stability of undoped and Mn-doped 2D core and core/shell NPLs was tested through a thermal annealing method described in the Supporting Information. The core NPLs have limited thermal stability and experienced thermal degradation causing the formation of larger NCs during annealing at 200 °C (Figures S7a and S8a), evidenced by a new broad PL peak (~430 nm) on the longer wavelength side of the NPL PL. More rapid degradation of core NPLs can be observed at higher annealing temperature, such as 220 °C (Figures S7b and S8b), resulting in a dominant red-shifted emission from the formation of large CdS NCs. However, the 2D core/shell NPLs showed no sign of degradation when annealed at 220 °C even after annealing for 3 h (Figures S7c and S8c), with no change in full width at half-maximum (fwhm) of either the CdS or Mn PL during the annealing process. Therefore, ZnS shell passivation using the SSSP method allows for both minimal NPL thermal degradation during shell coating and enhanced thermal stability of the resulting 2D core/shell NPLs.

Dopant (Mn^{2+}) position within the CdS host lattice was determined by X-band electron paramagnetic resonance (EPR) spectroscopy (Figure 2). In the 0.6% Mn:CdS NPLs, there are two sets of six-peak hyperfine splitting patterns with hyperfine constants of A = 94.3 and 68.6 G (Figure 2a), which represent the presence of the Mn²⁺ ions on the surface and within the

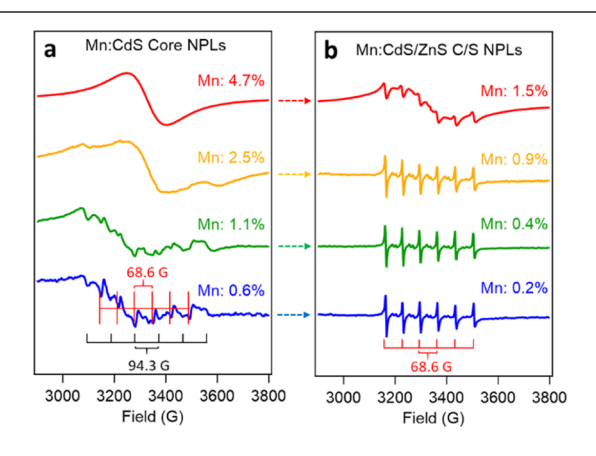


Figure 2. Dopant concentration-dependent X-band EPR spectra of (a) Mn:CdS core and (b) Mn:CdS/ZnS core/shell NPLs, showing an increase in dipolar contribution with increasing dopant concentration and a decrease in dipolar contribution as shelling occurs.

core lattice of CdS, respectively. 52,53 The broad dipolar peak visible in high-concentration samples is primarily due to strong short-range coupling between the paramagnetic Mn ions within close proximity to one another, which cause wide stretching bands and the elimination of hyperfine peaks. The loss of surface-indicative hyperfine peaks (*A* = 93.3 G) in core/shell NPLs further supports successful shelling (Figures 2b and S9), as formerly surface-doped Mn were either partially displaced or encapsulated by ZnS, effectively acting as coredoped Mn. The smaller dipolar contribution in the EPR spectra of the Mn:CdS/ZnS core/shell NPLs compared with that in the Mn:CdS core NPLs indicates a weaker short-range Mn—Mn interaction, which is consistent with decreased Mn concentration in core/shell NPLs from the ICP-OES measurements.

Figure 3a shows the normalized absorption and PL spectra of Mn:CdS NPLs during ZnS shell passivation up to 220 °C. The as-prepared Mn:CdS core NPLs exhibit an exciton absorption centered at 376 nm and CdS emission at 387 nm (fwhm: 11 nm). The band edge absorption position is consistent with 5-ML CdS NPLs (1.45 nm thickness) originally determined using the Pidgeon-Brown effective mass model by Ithurria et al. 50 However, no significant emission from Mn can be observed, which is quite surprising considering that the atomic energy levels of Mn²⁺ lie within the band gap of CdS, and should result in Mn PL as reported in many 0D Mn:CdS NCs.¹⁸ The PL QY of Mn:CdS NPLs was maintained at \sim 6% for all doping concentrations (Figure 3c). The absence of Mn PL in 2D Mn:CdS core NPLs may arise from overlap with the broad defect emission peak centered at ~540 nm and the low PL QY of the core NPLs (Figure 3a,c). In addition, the short exciton lifetime (a few nanoseconds as discussed below) and large exciton binding energy of 2D NPLs,⁵⁰ compared with corresponding 0D quantum dots, could lead to fast direct electron and hole combination, resulting in inefficient host-to-dopant energy transfer in the doped NPLs.

During ZnS shell passivation, a gradual enhancement of absorption in the UV range is observed in Mn:CdS/ZnS core/ shell NPLs because of the absorption of the ZnS shell. Remarkably, an enormous red shift of both the absorption and PL peak of the core/shell NPLs by ~420 meV (PL from 387 to 443 nm) was observed (Figure 3a,b). It should be noted that the value of the red shift is independent of doping concentration and is always ~420 meV for all the Mn:CdS/ ZnS core/shell NPLs in this study. This large spectral red shift is unexpected, considering the type I band alignment of the CdS/ZnS core/shell NPLs where both the excited electrons (in conduction band) and holes (in valence band) are confined within the CdS core, ⁵⁴ yet other, similarly large exciton energy shifts have been reported for 2D NCs. 55 For example, a large red shift up to 140 meV has been observed for 2D CdSe quantum belts after additional Cd(oleate), surface passivation, which electronically couples to the NC lattice and therefore increases the effective thickness of the nanobelts.⁵⁵ However, the ~420 meV red shift corresponds to the increasing of ~2-ML thickness of CdS, 50 which cannot be simply understood by the surface ligand effect. Though, it can be understood by the deposition of ~2 MLs of S on NPL surface Cd sites during ZnS shell passivation considering the same anion (S) in the CdS core and ZnS shell lattice, resulting in an increased effective core thickness of ~7 ML (Figure 4a). It should be noted that the exciton delocalization to the ZnS shell could be

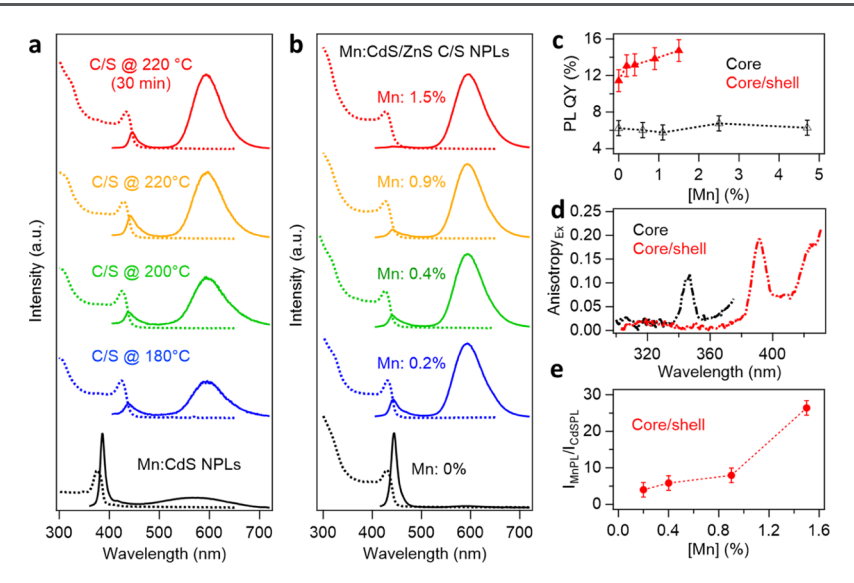


Figure 3. Normalized absorbance and emission spectra of (a) 0.6% Mn:CdS core NPLs shelled up to 220 °C using the SSSP method. (b) Dopant concentration-dependent absorbance and emission spectra of Mn:CdS/ZnS core/shell NPLs ([Mn]: 0–1.5%). (c) Total PL QY of core and core/shell-doped NPLs with respect to Mn concentration. (d) Excitation anisotropy data contingent on wavelength for 0.6% Mn:CdS core and corresponding 0.2% Mn:CdS/ZnS core/shell NPLs. (e) Peak intensity ratio of Mn PL with respect to the CdS host PL as a function of Mn concentration.

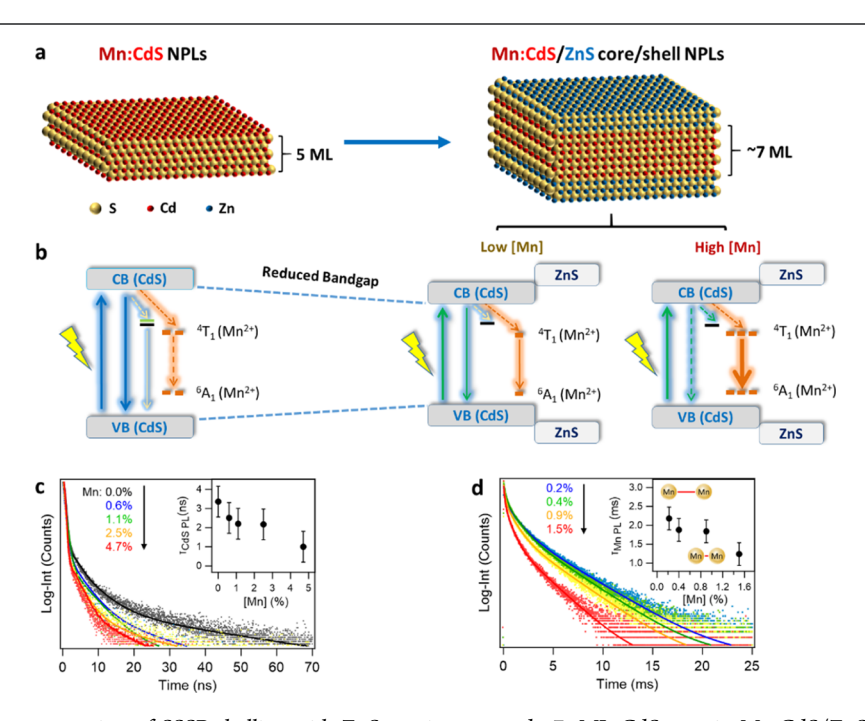


Figure 4. (a) Schematic representation of SSSP shelling with ZnS causing a pseudo-7- ML CdS core in Mn:CdS/ZnS core/shell NPLs. Orange spheres represent S ions, red spheres represent Cd ions, and blue spheres represent Zn ions. Mn is not shown for simplicity. (b) Representation of the CdS-Mn host-dopant energy transfer in Mn:CdS core and Mn:CdS/ZnS core/shell (with differing doping concentrations) NPLs. (c) CdS band gap PL lifetime for the Mn:CdS core NPLs as a function of Mn concentration (0-4.7%). (d) Mn PL lifetime of the Mn:CdS/ZnS core/shell NPLs as a function of Mn concentration (0-1.5%). Insets show the average lifetimes of the NPLs as a function of Mn concentration.

possible due to the large NPL quantum confinement along the thickness, even with the type I band alignment of the CdS/ZnS core/shell NPLs, and might contribute to the large spectra red shift observed upon ZnS coating.

Both the 2D Mn:CdS and Mn:CdS/ZnS core/shell NPLs show excitation anisotropy consistent with the nonspherical morphology of NPLs. Compared with Mn:CdS NPLs, shell passivation can provide an increased excitation anisotropy of Mn:CdS/ZnS core/shell NPLs for all dopant concentrations (Figures 3d and S10), which could be understood by the

increased rigidity of the Mn:CdS/ZnS core/shell NPLs. For the 2D Mn:CdS NPLs with a curved shape, a slightly different polarized emission corresponding to different directions could be obtained from multiple different positions within the 2D NPLs. Therefore, the lower excitation anisotropy of Mn:CdS NPLs might be due to the effective cancelling of the polarized emission from the curved structure of the ultrathin NPLs.

Intriguingly, the growth of the ZnS shell on Mn:CdS NPLs can "turn on" a distinct Mn emission band centered at ${\sim}600$ nm ($^4T_1 \rightarrow {}^6A_1$ d–d transition) (Figure 3a,b). The Mn

emission can be discerned almost immediately once the ZnS shelling temperature reaches 120 °C, followed by narrowing of the Mn²⁺ emission peak at 160 °C (Figure S11). The narrowing of the Mn emission indicates successful ZnS surface passivation to effectively remove surface defect and the corresponding defect emission (Figure S11). Additionally, it appears that increasing the dopant concentration correlates with a more rapid narrowing of the Mn emission, primarily due to a more prominent Mn emission from increased host-dopant energy transfer, even early in the shelling process. The appearance of Mn PL indicates that the host-dopant energy transfer is favored in the core/shell NPLs, which could be attributed to a larger effective CdS core with less quantum confined exciton in the core/shell NPLs, along with the efficient removal of surface defect states via ZnS shell passivation (Figure 4a,b).

Figure 3b displays the normalized absorbance and PL of 2D Mn:CdS/ZnS NPLs with Mn concentrations of 0, 0.2, 0.4, 0.9, and 1.5%. A distinct trend can be observed in which an increased intensity ratio of Mn to CdS PL can be obtained as the Mn concentration increases (Figure 3e). In addition, the PL QY of the core/shell NPLs increases with Mn concentration from ~11% at 0% Mn to ~15% at 1.5% Mn (Figure 3c), which indicates more efficient host—dopant energy transfer with doping concentration caused by the removal of defect sites in the core/shell NPLs. The host—dopant energy transfer from the CdS—Mn coupling can be qualitatively monitored by the PL intensity ratio of Mn dopant and CdS host NCs as indicated by eq 1¹⁸

$$\frac{I_{\rm Mn}}{I_{\rm NC}} \propto \frac{K_{\rm ET}}{K_{\rm r}^{\rm NC}} \tag{1}$$

where increased PL intensity ratio of dopant $(I_{\rm Mn})$ to host $(I_{\rm NC})$ intensity is proportional to increased energy-transfer relaxation rates $(K_{\rm ET})$ with respect to the relaxation rate of the host lattice $(K_{\rm r}^{\rm NC})$. The increased relative Mn PL intensity with increased Mn concentration is consistent with higher host–dopant energy-transfer efficiency from the CdS host lattice to the doped Mn energy states (Figure 4b), which can be qualitatively understood by increasing the number of acceptors interacting with a given donor. Effectively, more energy-transfer pathways are available, leading to an increased transfer rate and efficiency.

It should be noted that energy transfer between CdS host lattice and Mn dopant is very complicated in the presence of defect states. To further verify the doping concentration-dependent host-to-dopant energy transfer, we performed PL lifetime measurements of the NPLs. The energy-transfer efficiency (Φ_{ET}) can be also represented with respect to the host PL decay lifetime (τ_{D}) and undoped radiative decay lifetime (τ_{UD}) as in eq 2^{19}

$$\tau_{\rm D} = \tau_{\rm UD}(1 - \Phi_{\rm ET}) \tag{2}$$

in which the CdS PL decay lifetime $(\tau_{\rm D})$ of doped NPLs is represented with respect to the undoped NPL radiative decay lifetime $(\tau_{\rm UD})$ and the rate of energy-transfer efficiency, $\Phi_{\rm ET}$. Equation 2 indicates that the CdS host PL decay lifetime is inversely proportional to the host-to-dopant energy-transfer efficiency $(\Phi_{\rm ET})$. Indeed, the CdS PL lifetime of Mn:CdS NPLs (Figure 4c and Table S1) decreases with increasing dopant concentration, supporting the increased rate of host-dopant energy transfer. In addition, decreased Mn PL lifetime

with increased doping concentration (Figure 4d and Table S1) can be observed, which is due to "concentration quenching" from short-range Mn–Mn interactions at higher doping concentrations.¹⁹

To gain further insights into the Mn–Mn interaction as well as magnetic properties of these doped 2D NPLs, we measured the isothermal magnetization of the Mn:CdS and Mn:CdS/ZnS NPLs as a function of doping concentration (Figure 5). It

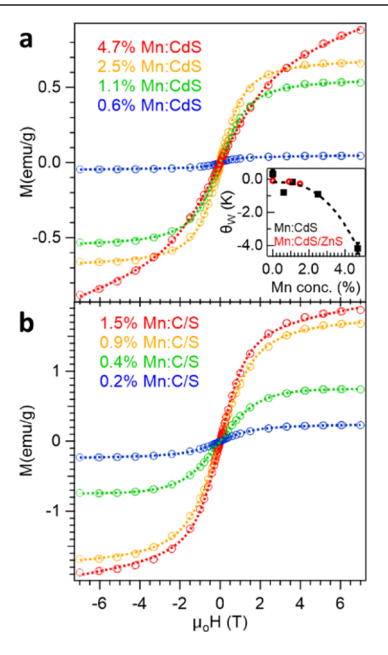


Figure 5. Isothermal magnetization (T = 2 K) for (a) Mn:CdS and (b) Mn:CdS/ZnS NPLS as a function of Mn concentration. The dashed lines are Brillouin fits to the data points (expressed as open circles). Inset in (a): Weiss temperatures (from magnetic susceptibility fits) as a function of Mn concentration. The lines are a guide for the eyes.

is important to note that both the core and core/shell NPLs show weak paramagnetism for the undoped samples, suggestive of intrinsic spin states in these 2D materials. Both the core-only and core/shell NPLs exhibit systematic increases in saturation magnetization, M_{st} as a function of Mn concentration (Figure 5). For 0.6% Mn:CdS NPLs, we observe an effective magnetic moment, $\mu_{\rm eff}$ = 6 $\mu_{\rm B}/{\rm Mn}$, matching the expected spin-only moment for Mn²⁺. For higher doped CdS NPLs, the values of $\mu_{\rm eff}$ range between 2 and 4 $\mu_{\rm B}/{\rm Mn}$, suggesting competing magnetic interactions, possibly because of interactions with surface states. 12,56 The highest doped CdS NPLs (Mn = 4.7%) does not exhibit magnetic saturation at fields as high as 7 T, suggesting complex magnetic interactions, perhaps because of antiferromagnetic exchange. Magnetic susceptibility (χ) data suggests paramagnetism for all the samples, with no obvious magnetic phase transitions in the zero-field or field-cooled scans (Figure S12). Fits of the data to a modified Curie-Weiss law as in eq 3

$$\chi = \chi_0 + \frac{C}{(T - \theta_{\rm W})} \tag{3}$$

where χ_0 is the temperature-independent contribution of the magnetic susceptibility and θ_W is the Weiss temperature, showing increasingly negative values of θ_W as a function of doping concentration in Mn:CdS NPLs (Figure 5a insert),

which suggests increased antiferromagnetic interactions with Mn concentration. This observation is consistent with the absence of magnetic saturation in the 4.7% Mn:CdS NPLs (Figure 5a). For all Mn:CdS/ZnS core/shell NPLs, we observe both magnetic saturation behavior at high field (Figure 5b) and minor changes in the Weiss temperature ($\theta_{\rm W}$) (Figure 5a inset). This can be understood by considering reduced antiferromagnetic interactions in the doped core/shell NPLs, resulting from lower doping concentrations coupled with a reduction of surface defects in the Mn:CdS/ZnS core/shell NPLs.

CONCLUSIONS

In conclusion, we have developed a one-pot wet chemistry method for the synthesis of 2D Mn:CdS NPLs. To improve the thermal stability and optical properties, we further grew ZnS shell-passivated Mn:CdS/ZnS core/shell NPLs using a SSSP method at a moderate temperature. Both EPR and XRD measurements confirm successful Mn doping inside the CdS NPL lattice. Although no significant dopant emission was observed in 2D Mn:CdS NPLs, the Mn:CdS/ZnS core/shell NPLs show tunable PL from the host NPLs and the Mn²⁺ dopant with doping concentration, as well as an enormous red shift of both the absorption and PL peak by ~420 meV. Decreases in both CdS host and Mn PL lifetime with doping concentration are consistent with increasing host-dopant energy-transfer efficiency and Mn-Mn interactions with higher dopant concentration. Magnetic measurements suggest paramagnetism in all the studied samples, with antiferromagnetic coupling increasing with dopant concentration and decreasing with the formation of the ZnS shell. Applications for these materials are vast, as they can be tuned for a specific function, such as in photovoltaics, polarized light-emitting diodes, as dilute magnetic semiconductors, or as giant oscillator strength transistors. 31–34,57

■ EXPERIMENTAL SECTION

Chemicals. Zinc diethyldithiocarbamate (97%, Zn(DDTC)₂, Aldrich), oleylamine (70%, OAm, Aldrich), ethanol (99.5%, EtOH, VWR), hexanes (98.5%, VWR), methanol (99.8%, MeOH, VWR), toluene (>99.8%, VWR), 1-octadecene (90%, ODE, Alfa), tetradecanoic acid (98.0%, H(Myr), Alfa), sodium hydroxide (99.6%, NaOH, Fisher), cadmium nitrate tetrahydrate (99.0%, Aldrich), sulfur (99.5%, Alfa), zinc acetate dihydrate (98.0–101.0%, Zn(OAc)₂, Alfa), and chloroform (99.8%, VWR) were used without any further purification.

Synthesis of Cadmium Myristate. A 0.025 M sodium myristate solution was prepared by dissolving 240 mg (6.0 mmol) of sodium hydroxide and 1.370 g (6.0 mmol) of myristic acid in 240 mL of methanol in a 500 mL Erlenmeyer flask (E-flask). Separately, dissolve 617 mg (2.0 mmol) of cadmium nitrate tetrahydrate in 40 mL of methanol in a 100 mL E-flask. Add the cadmium nitrate solution dropwise (~1 drop/s) to the stirring sodium myristate solution, resulting in the formation of a white precipitate of cadmium myristate. Wash the resulting precipitate three times with 50–100 mL of methanol and then dry under vacuum overnight.

Sulfur–Octadecene Solution. A 0.1 M sulfur–octadecene (SODE) solution was prepared by dissolving 48 mg (1.5 mmol) of sulfur in 15 mL of ODE by sonication for at least 2 h. This solution was prepared the same day on which a reaction took place.

was prepared the same day on which a reaction took place. **Synthesis of Mn:CdS NPLs.** For a typical synthesis of 2D Mn:CdS NPLs, a solution containing 113.4 mg (0.20 mmol) of Cd(myr)₂, 43.9 mg (0.20 mmol) of Zn(OAc)₂, 1.0 mL of S-ODE, and 9.0 mL of ODE was prepared in a 25 mL three-neck round-bottom flask. Degas the solution for 30 min at room temperature and another 30 min at 100 °C. Afterward, cool the reaction to room temperature

under argon. Inject $Mn(NO_3)_2$ in minimal MeOH into the solution. Degas the solution at room temperature for 30 min and another 30 min at 100 °C. Heat the reaction mixture to 200 °C and maintain that temperature for 1 h under argon. Cool the reaction to room temperature and add \sim 6 mL of toluene into the resulting reaction solution (\sim 10 mL). Centrifuge the solution at 5000 rpm for 2 min to remove any unreacted precursor, if the solution is visibly cloudy. Use a small aliquot of the solution for optical measurements. Precipitate the Mn:CdS NPLs out of solution by adding 3–4 mL of ethanol followed by centrifugation at 5000 rpm for 2 min. Dissolve the precipitate in minimal hexane after removing the supernatant for the synthesis of Mn:CdS/ZnS core/shell NPLs. For XRD and TEM measurements, clean the product three to four times using minimal toluene/EtOH followed by centrifugation.

Synthesis of Mn:CdŚ/ZnS Core/Shell NPLs via the SSSP Method. In a 25 mL three-neck round-bottom flask, add the previously synthesized Mn:CdS NPLs in hexane, 6.0 mL ODE, 2.0 mL OAm, and 145 mg (0.40 mmol) Zn(DDTC)₂. Degas the mixture at 50 °C for 30 min and at 70 °C for an additional 30 min. Increase the reaction temperature slowly to 220 °C at a rate of ~5 °C/min and maintained at 220 °C for 0.5—3 h for ZnS shell coating on the surface of Mn:CdS NPLs. Then, cool the reaction to room temperature naturally. Clean the core/shell NPLs similarly to those of the core NPLs using toluene and EtOH.

Sample Characterization. TEM measurements were performed on an FEI T12 Twin TEM operated at 120 kV with a LaB6 filament and Gatan Orius dual-scan CCD camera. AFM images were collected on a Bruker Innova SPM instrument housed on a TMC vibration isolation table and utilized tapping mode and silicon MikroMasch noncontact cantilever probes (HQ:NSC14). Samples were drop-cast onto freshly cleaved highly ordered pyrolitic graphite and vacuumdried. Powder XRD patterns were recorded on a Bruker D2 Phaser with a LYKXEYE 1D silicon strip detector using Cu K α radiation (λ = 1.5406 Å). The UV-visible spectrophotometry (UV-vis) measurements were collected on an Agilent Cary 60 spectrophotometer. Steady-state and time-resolved emission spectra were recorded using an Edinburgh FLS-980 spectrometer with a photomultiplier tube (PMT, R928 Hamamatsu) detector. ICP-OES elemental composition analysis was performed on a PerkinElmer Optima 3300DV. Roomtemperature X-band EPR spectra were recorded at a microwave frequency of 9.8 GHz on a Bruker ELEXSYSII E500 spectrometer. Magnetic susceptibilities were measured in the temperature range 2-300 K under an applied magnetic field of 0.1 T and isothermal magnetization measurements were performed from -7 to 7 T at 2 K on a Quantum Design MPMS-XL-7 SQUID magnetometer.

ASSOCIATED CONTENT

S Supporting Information

The Supporting Information is available free of charge on the ACS Publications website at DOI: 10.1021/acs.chemmater.9b00006.

Experimental details, all characterization data (TEM, AFM, XRD, lifetime, and EPR), optical data (absorption, PL, and excitation anisotropy spectra) and magnetic susceptibility for all samples at tested temperature, and doping concentrations as well as control experiments (PDF)

AUTHOR INFORMATION

Corresponding Author

*E-mail: wzhen104@syr.edu.

ORCID ®

Mathew M. Maye: 0000-0002-5320-1071 Weiwei Zheng: 0000-0003-1394-1806

Notes

The authors declare no competing financial interest.

ACKNOWLEDGMENTS

W.Z. acknowledges the support from the start-up grant of Syracuse University and ACS-PRF (no. 59861-DNIS). TEM measurements were performed at the Cornell Center for Materials Research (CCMR), which are supported through the NSF MRSEC program (DMR-1719875). ACERT is supported by the National Institutes of Health Grant NIH/NIBIB R010EB00315. We thank D. A. Driscoll at SUNY-ESF for helping with ICP-OES measurements. R.W.M. acknowledges the support by the National Science Foundation under grant no. DMR-1708617.

REFERENCES

- (1) Achtstein, A. W.; Prudnikau, A. V.; Ermolenko, M. V.; Gurinovich, L. I.; Gaponenko, S. V.; Woggon, U.; Baranov, A. V.; Leonov, M. Y.; Rukhlenko, I. D.; Fedorov, A. V.; Artemyev, M. V. Electroabsorption by 0D, 1D, and 2D nanocrystals: a comparative study of CdSe colloidal quantum dots, nanorods, and nanoplatelets. *ACS Nano* **2014**, *8*, 7678–7686.
- (2) Ithurria, S.; Bousquet, G.; Dubertret, B. Continuous transition from 3D to 1D confinement observed during the formation of CdSe nanoplatelets. *J. Am. Chem. Soc.* **2011**, *133*, 3070–3077.
- (3) Sitt, A.; Even-Dar, N. a.; Halivni, S.; Faust, A.; Yedidya, L.; Banin, U. Analysis of Shape and Dimensionality Effects on Fluorescence Resonance Energy Transfer from Nanocrystals to Multiple Acceptors. *J. Phys. Chem. C* **2013**, *117*, 22186–22197.
- (4) Hodes, G. When Small Is Different: Some Recent Advances in Concepts and Applications of Nanoscale Phenomena. *Adv. Mater.* **2007**, *19*, 639–655.
- (5) Xia, Y.; Xiong, Y.; Lim, B.; Skrabalak, S. E. Shape-Controlled Synthesis of Metal Nanocrystals: Simple Chemistry Meets Complex Physics? *Angew. Chem., Int. Ed.* **2009**, *48*, 60–103.
- (6) Peng, X.; Manna, L.; Yang, W.; Wickham, J.; Scher, E.; Kadavanich, A.; Alivisatos, A. P. Shape control of CdSe nanocrystals. *Nature* **2000**, *404*, 59–61.
- (7) Murray, C. B.; Norris, D. J.; Bawendi, M. G. Synthesis and characterization of nearly monodisperse CdE (E = sulfur, selenium, tellurium) semiconductor nanocrystallites. *J. Am. Chem. Soc.* **1993**, *115*, 8706–8715.
- (8) Yin, Y.; Alivisatos, A. P. Colloidal nanocrystal synthesis and the organic-inorganic interface. *Nature* **2005**, *437*, 664–670.
- (9) Mokari, T.; Rothenberg, E.; Popov, I.; Costi, R.; Banin, U. Selective Growth of Metal Tips onto Semiconductor Quantum Rods and Tetrapods. *Science* **2004**, *304*, 1787–1790.
- (10) Mocatta, D.; Cohen, G.; Schattner, J.; Millo, O.; Rabani, E.; Banin, U. Heavily Doped Semiconductor Nanocrystal Quantum Dots. *Science* **2011**, 332, 77–81.
- (11) Beaulac, R.; Schneider, L.; Archer, P. I.; Bacher, G.; Gamelin, D. R. Light-Induced Spontaneous Magnetization in Doped Colloidal Quantum Dots. *Science* **2009**, 325, 973–976.
- (12) Zheng, W.; Strouse, G. F. Involvement of Carriers in the Size-Dependent Magnetic Exchange for Mn:CdSe Quantum Dots. *J. Am. Chem. Soc.* **2011**, *133*, 7482–7489.
- (13) Zheng, W.; Singh, K.; Wang, Z.; Wright, J. T.; van Tol, J.; Dalal, N. S.; Meulenberg, R. W.; Strouse, G. F. Evidence of a ZnCr₂Se₄ Spinel Inclusion at the Core of a Cr-Doped ZnSe Quantum Dot. *J. Am. Chem. Soc.* **2012**, *134*, 5577–5585.
- (14) Zheng, W.; Kumar, P.; Washington, A.; Wang, Z.; Dalal, N. S.; Strouse, G. F.; Singh, K. Quantum Phase Transition from Superparamagnetic to Quantum Superparamagnetic State in Ultrasmall Cd_{1-x}Cr(II)_xSe Quantum Dots? *J. Am. Chem. Soc.* **2012**, *134*, 2172–2179.
- (15) Kittilstved, K. R.; Gamelin, D. R. Activation of High-TC Ferromagnetism in Mn²⁺-Doped ZnO using Amines. *J. Am. Chem. Soc.* **2005**, *127*, 5292–5293.
- (16) Chen, O.; Shelby, D. E.; Yang, Y.; Zhuang, J.; Wang, T.; Niu, C.; Omenetto, N.; Cao, Y. C. Excitation-intensity-dependent color-

tunable dual emissions from manganese-doped CdS/ZnS core/shell nanocrystals. *Angew. Chem., Int. Ed. Engl.* **2010**, 49, 10132–10135.

- (17) Yu, J. H.; Liu, X.; Kweon, K. E.; Joo, J.; Park, J.; Ko, K.-T.; Lee, D. W.; Shen, S.; Tivakornsasithorn, K.; Son, J. S.; Park, J.-H.; Kim, Y.-W.; Hwang, G. S.; Dobrowolska, M.; Furdyna, J. K.; Hyeon, T. Giant Zeeman splitting in nucleation-controlled doped CdSe:Mn²⁺ quantum nanoribbons. *Nat. Mater.* **2010**, *9*, 47–53.
- (18) Hofman, E.; Robinson, R. J.; Li, Z.-J.; Dzikovski, B.; Zheng, W. Controlled Dopant Migration in CdS/ZnS Core/Shell Quantum Dots. J. Am. Chem. Soc. 2017, 139, 8878–8885.
- (19) Li, Z.-J.; Hofman, E.; Blaker, A.; Davis, A. H.; Dzikovski, B.; Ma, D.-K.; Zheng, W. Interface Engineering of Mn-Doped ZnSe-Based Core/Shell Nanowires for Tunable Host–Dopant Coupling. *ACS Nano* **2017**, *11*, 12591–12600.
- (20) Deng, Z.; Tong, L.; Flores, M.; Lin, S.; Cheng, J.-X.; Yan, H.; Liu, Y. High-quality manganese-doped zinc sulfide quantum rods with tunable dual-color and multiphoton emissions. *J. Am. Chem. Soc.* **2011**, *133*, 5389–5396.
- (21) Nag, A.; Chakraborty, S.; Sarma, D. D. To Dope Mn²⁺ in a Semiconducting Nanocrystal. *J. Am. Chem. Soc.* **2008**, *130*, 10605–10611.
- (22) Li, Z.-J.; Hofman, E.; Davis, A. H.; Khammang, A.; Wright, J. T.; Dzikovski, B.; Meulenberg, R. W.; Zheng, W. Complete Dopant Substitution by Spinodal Decomposition in Mn-Doped Two-Dimensional CsPbCl3 Nanoplatelets. *Chem. Mater.* **2018**, *30*, 6400–6409.
- (23) Liu, W.; Lin, Q.; Li, H.; Wu, K.; Robel, I.; Pietryga, J. M.; Klimov, V. I. Mn²⁺-Doped Lead Halide Perovskite Nanocrystals with Dual-Color Emission Controlled by Halide Content. *J. Am. Chem. Soc.* **2016**, 138, 14954–14961.
- (24) Guria, A. K.; Dutta, S. K.; Adhikari, S. D.; Pradhan, N. Doping Mn²⁺ in Lead Halide Perovskite Nanocrystals: Successes and Challenges. *ACS Energy Lett.* **2017**, *2*, 1014–1021.
- (25) Bryan, J. D.; Gamelin, D. R. Doped Semiconductor Nanocrystals: Synthesis, Characterization, Physical Properties, and Applications. *Progress in Inorganic Chemistry*; Wiley Online Library, 2005; Vol. 54, pp 47–126.
- (26) Buonsanti, R.; Milliron, D. J. Chemistry of Doped Colloidal Nanocrystals. *Chem. Mater.* **2013**, 25, 1305–1317.
- (27) Norris, D. J.; Efros, A. L.; Erwin, S. C. Doped nanocrystals. *Science* **2008**, *319*, 1776–1779.
- (28) Wolf, S. A.; Awschalom, D. D.; Buhrman, R. A.; Daughton, J. M.; von Molnár, S.; Roukes, M. L.; Chtchelkanova, A. Y.; Treger, D. M. Spintronics: A Spin-Based Electronics Vision for the Future. *Science* **2001**, *294*, 1488–1495.
- (29) Beaulac, R.; Archer, P. I.; Ochsenbein, S. T.; Gamelin, D. R. Mn(2+)-Doped CdSe Quantum Dots: New Inorganic Materials for Spin-Electronics and Spin-Photonics. *Adv. Funct. Mater.* **2008**, *18*, 3873–3891.
- (30) Erickson, C. S.; Bradshaw, L. R.; McDowall, S.; Gilbertson, J. D.; Gamelin, D. R.; Patrick, D. L. Zero-Reabsorption Doped-Nanocrystal Luminescent Solar Concentrators. *ACS Nano* **2014**, *8*, 3461–3467.
- (31) Diroll, B. T.; Talapin, D. V.; Schaller, R. D. Violet-to-Blue Gain and Lasing from Colloidal CdS Nanoplatelets: Low-Threshold Stimulated Emission Despite Low Photoluminescence Quantum Yield. ACS Photonics 2017, 4, 576–583.
- (32) Pelton, M. Carrier Dynamics, Optical Gain, and Lasing with Colloidal Quantum Wells. J. Phys. Chem. C 2018, 122, 10659–10674.
- (33) Pelzer, K. M.; Darling, S. B.; Gray, S. K.; Schaller, R. D. Exciton size and quantum transport in nanoplatelets. *J. Chem. Phys.* **2015**, *143*, 224106.
- (34) Tessier, M. D.; Spinicelli, P.; Dupont, D.; Patriarche, G.; Ithurria, S.; Dubertret, B. Efficient exciton concentrators built from colloidal core/crown CdSe/CdS semiconductor nanoplatelets. *Nano Lett.* **2014**, *14*, 207–213.
- (35) Kormilina, T. K.; Cherevkov, S. A.; Fedorov, A. V.; Baranov, A. V. Cadmium Chalcogenide Nano-Heteroplatelets: Creating Advanced Nanostructured Materials by Shell Growth. *Small* **2017**, *13*, 1702300.

(36) Pradhan, N.; Peng, X. Efficient and Color-Tunable Mn-Doped ZnSe Nanocrystal Emitters: Control of Optical Performance via Greener Synthetic Chemistry. J. Am. Chem. Soc. 2007, 129, 3339—3347

- (37) Yang, Y.; Chen, O.; Angerhofer, A.; Cao, Y. C. On Doping CdS/ZnS Core/Shell Nanocrystals with Mn. J. Am. Chem. Soc. 2008, 130, 15649–15661.
- (38) Meulenberg, R. W.; van Buuren, T.; Hanif, K. M.; Willey, T. M.; Strouse, G. F.; Terminello, L. J. Structure and composition of Cudoped CdSe nanocrystals using soft X-ray absorption spectroscopy. *Nano Lett.* **2004**, *4*, 2277–2285.
- (39) Kato, F.; Kittilstved, K. R. Site-Specific Doping of Mn2+ in a CdS-Based Molecular Cluster. *Chem. Mater.* **2018**, 30, 4720–4727.
- (40) Vlaskin, V. A.; Barrows, C. J.; Erickson, C. S.; Gamelin, D. R. Nanocrystal Diffusion Doping. *J. Am. Chem. Soc.* **2013**, *135*, 14380–14389.
- (41) Delikanli, S.; Akgul, M. Z.; Murphy, J. R.; Barman, B.; Tsai, Y.; Scrace, T.; Zhang, P.; Bozok, B.; Hernández-Martínez, P. L.; Christodoulides, J.; Cartwright, A. N.; Petrou, A.; Demir, H. V. Mn²⁺-Doped CdSe/CdS Core/Multishell Colloidal Quantum Wells Enabling Tunable Carrier—Dopant Exchange Interactions. *ACS Nano* **2015**, *9*, 12473—12479.
- (42) Muckel, F.; Delikanli, S.; Hernández-Martínez, P. L.; Priesner, T.; Lorenz, S.; Ackermann, J.; Sharma, M.; Demir, H. V.; Bacher, G. sp—d Exchange Interactions in Wave Function Engineered Colloidal CdSe/Mn:CdS Hetero-Nanoplatelets. *Nano Lett.* **2018**, *18*, 2047—2053.
- (43) Fainblat, R.; Frohleiks, J.; Muckel, F.; Yu, J. H.; Yang, J.; Hyeon, T.; Bacher, G. Quantum Confinement-Controlled Exchange Coupling in Manganese(II)-Doped CdSe Two-Dimensional Quantum Well Nanoribbons. *Nano Lett.* **2012**, *12*, 5311–5317.
- (44) Erwin, S. C.; Zu, L.; Haftel, M. I.; Efros, A. L.; Kennedy, T. A.; Norris, D. J. Doping semiconductor nanocrystals. *Nature* **2005**, *436*, 91–94.
- (45) Mikulec, F. V.; Kuno, M.; Bennati, M.; Hall, D. A.; Griffin, R. G.; Bawendi, M. G. Organometallic Synthesis and Spectroscopic Characterization of Manganese-Doped CdSe Nanocrystals. *J. Am. Chem. Soc.* **2000**, *122*, 2532–2540.
- (46) Zu, L.; Norris, D. J.; Kennedy, T. A.; Erwin, S. C.; Efros, A. L. Impact of ripening on manganese-doped ZnSe nanocrystals. *Nano Lett.* **2006**, *6*, 334–340.
- (47) Rowland, C. E.; Fedin, I.; Diroll, B. T.; Liu, Y.; Talapin, D. V.; Schaller, R. D. Elevated Temperature Photophysical Properties and Morphological Stability of CdSe and CdSe/CdS Nanoplatelets. *J. Phys. Chem. Lett.* **2018**, *9*, 286–293.
- (48) Chen, D.; Zhao, F.; Qi, H.; Rutherford, M.; Peng, X. Bright and Stable Purple/Blue Emitting CdS/ZnS Core/Shell Nanocrystals Grown by Thermal Cycling Using a Single-Source Precursor. *Chem. Mater.* **2010**, *22*, 1437–1444.
- (49) Polovitsyn, A.; Dang, Z.; Movilla, J. L.; Martín-García, B.; Khan, A. H.; Bertrand, G. H. V.; Brescia, R.; Moreels, I. Synthesis of Air-Stable CdSe/ZnS Core—Shell Nanoplatelets with Tunable Emission Wavelength. *Chem. Mater.* **2017**, *29*, 5671–5680.
- (50) Ithurria, S.; Tessier, M. D.; Mahler, B.; Lobo, R. P. S. M.; Dubertret, B.; Efros, A. L. Colloidal nanoplatelets with two-dimensional electronic structure. *Nat. Mater.* **2011**, *10*, 936–941.
- (51) Ithurria, S.; Bousquet, G.; Dubertret, B. Continuous Transition from 3D to 1D Confinement Observed during the Formation of CdSe Nanoplatelets. *J. Am. Chem. Soc.* **2011**, *133*, 3070–3077.
- (52) Zheng, W.; Wang, Z.; Wright, J.; Goundie, B.; Dalal, N. S.; Meulenberg, R. W.; Strouse, G. F. Probing the Local Site Environments in Mn:CdSe Quantum Dots. J. Phys. Chem. C 2011, 115, 23305–23314.
- (53) Zheng, W.; Wang, Z.; van Tol, J.; Dalal, N. S.; Strouse, G. F. Alloy Formation at the Tetrapod Core/Arm Interface. *Nano Lett.* **2012**, *12*, 3132–3137.
- (54) Reiss, P.; Protière, M.; Li, L. Core/Shell Semiconductor Nanocrystals. *Small* **2009**, *5*, 154–168.

(55) Zhou, Y.; Wang, F.; Buhro, W. E. Large Exciton Energy Shifts by Reversible Surface Exchange in 2D II–VI Nanocrystals. *J. Am. Chem. Soc.* **2015**, *137*, 15198–15208.

- (56) Meulenberg, R. W.; Lee, J. R. I.; McCall, S. K.; Hanif, K. M.; Haskel, D.; Lang, J. C.; Terminello, L. J.; van Buuren, T. Evidence for Ligand-Induced Paramagnetism in CdSe Quantum Dots. *J. Am. Chem. Soc.* **2009**, *131*, 6888–6889.
- (57) Li, M.; Zhi, M.; Zhu, H.; Wu, W. Y.; Xu, Q. H.; Jhon, M. H.; Chan, Y. Ultralow-threshold multiphoton-pumped lasing from colloidal nanoplatelets in solution. *Nat. Commun.* **2015**, *6*, 8513.